Digital Particle Imaging Velocimetry of Viscoelastic Fluids

Peyman Pakdel and Gareth H. McKinley
Div. of Engineering and Applied Sciences, Harvard University, Cambridge, MA 02138

We investigate the utility of digital particle imaging velocimetry (DPIV) for performing kinematic measurements in non-Newtonian flows. With the advances in numerical techniques for simulation of viscoelastic flows, acquisition of spatially dense 2-D kinematic data in steady and time-dependent deformations can be useful in verifying predictions of the corresponding computational studies. Furthermore, kinematic measurements of the velocity field and rate of deformation in prototypical industrial processes can significantly enhance the rational design and optimization of polymer processing unit operations. Application of a high seeding density DPIV technique in viscoelastic media is discussed, and quantitative data are obtained in a number of industrially relevant flow geometries. The issues of velocity-position assignment and the effects of a velocity gradient across DPIV correlation regions are discussed. A simple yet effective averaging technique preserves the order of accuracy and assigns the velocity vectors to their appropriate positions using an overlapping discretization scheme. The examples studied experimentally include steady flow in circular pipes, flow past obstructions, flow in a lid-driven cavity, and time-dependent free-surface extensional flows in a liquid filament. With the exception of the first example, these flow geometries constitute an important collection of configurations in which quantitative experimental data for non-Newtonian fluids are scarce or nonexistent.

Introduction

Processing of polymeric materials has been the subject of significant interest in the chemical industry during the past 50 years. One of the main objectives of polymer engineering research is to increase the predictive capabilities with respect to the effects of processing variables, microstructure, and the environment on ultimate material properties (Federal Coordinating Council, 1993). Progress toward these goals requires a clear understanding of material behavior under various flow and processing conditions.

Macroscopic modeling efforts for macromolecular fluids and materials are partly directed at the derivation of constitutive equations that provide a functional relationship between the local stress and the rate of deformation. These constitutive models introduce fundamental material parameters that need to be determined for a specific fluid via rheological measurements. Although broad qualitative agreements with the predictions of constitutive models exist, quantitative agreement over a wide range of materials and processing conditions is yet to be reached, particularly under transient conditions (Bird et al., 1987). Accurate numerical prediction of transport phenomena in model problems depends strongly on the type of constitutive model used in the problem formulation (Rajagopalan et al., 1996). Qualitative predictions of the flow evolution with increasing flow rate are possible in certain well-studied cases; however, numerical simulations and experimental observations of flow characteristics often differ by orders of magnitude (Crochet, 1988).

Accurate experimental measurements are essential ingredients for progress in our understanding of the deformation behavior of complex fluids. To develop a predictive capability for a particular process, given a set of defining parameters (e.g., temperature, flow rate, and operating pressure), it is essential to probe the local dynamic evolution and deformation history of material elements within the flow domain. Evaluation of the local velocity field, and subsequently the rate of deformation, have been important goals in various ex-

perimental fluid mechanical techniques; however, many of the classic techniques cannot be used in non-Newtonian-fluid media because existing correlations or dynamical assumptions intrinsic to the measuring technique fail as a result of the constitutive nonlinearities of the material deformation. Yet as accurate computation of more complicated flow geometries becomes increasingly feasible, reliable and spatially dense kinematic data of the corresponding flow fields are needed for the purpose of quantitative comparisons. These observations motivate research and development of new experimental techniques that facilitate and accommodate *planar* as opposed to *pointwise* measurements. Digital imaging technology within the chemical engineering community has received significant attention in recent years since it provides a noninvasive tool for measuring kinematic and statistical quantities, for example, in multiphase media (see, e.g., Chen et al., 1995; Scheller and Bousfield, 1995). As we demonstrate in this article, digital image acquisition in conjunction with image-processing calculations can serve to provide important two-dimensional (2-D) kinematic data quantifying deformation history in viscoelastic materials.

To qualitatively observe velocity fields in the bulk of a deforming fluid medium, flow visualization is typically employed in a vast majority of experiments. A laser or other focused light source is used in conjunction with a cylindrical lens to form an intense light sheet that illuminates planar cross sections of axisymmetric or three-dimensional (3-D) flows. Long photographic exposures lead to streak photographs, in which the records of a large number of particle tracks with a given Lagrangian velocity lead to an approximate representation of the streamlines of the corresponding Eulerian velocity field (Binding et al., 1987). The applications of this technique to non-Newtonian-fluid motion have been extremely broad and are summarized in the album assembled by Boger and Walters (1993). A quantitative improvement in measurements of the velocity field can be made by the use of laser doppler velocimetry (LDV). Although accurate and noninvasive, LDV systems are prohibitively expensive and poorly suited to industrial test environments outside a research facility. Furthermore the velocity measurements are obtained on a pointwise basis and the extent of data acquisition during an experimental run is limited (e.g., McKinley et al., 1991), especially if the flow of interest is transient in nature.

A major improvement can be made by employing digital particle image velocimetry (DPIV) (Cho, 1989; Willert and Gharib, 1991). In this technique, the fluid is seeded with $O(\mu m)$ size particles at very low concentrations. The spatial displacements of small particles are then recorded by successive image exposures that are separated by a small time interval. Every image is subdivided into small interrogation regions in which particles are assumed to move with a constant velocity. Using the cross-correlation technique, the "average" 2-D displacement at every interrogation region is calculated, after which division by the time increment Δt gives an accurate estimate of the vectorial velocity components in the imaging plane. An extensive review of methods that utilize particle and speckle image velocimetry is given by Adrian (1991) and in the more recent work of Buchhave (1992).

The DPIV system relies on the accuracy of the image-processing calculations. Every image is subdivided into small interrogation regions or "subimages" and the cross-correlation function for each pair of successive subimages is calculated using the fast Fourier transform (FFT) (Brigham, 1974). To ensure that each interrogation region contains a reasonable number of tracer particles, the subimages overlap with their neighbors.

Considering a typical image of 640×480 pixels with overlapping interrogation regions of 32×32 pixels and a temporal data rate of 30 frames per second, a DPIV algorithm requires approximately 1 GFLOPS for real-time analysis. Although the data processing of a DPIV experiment is extensive, the technique provides time-resolved, spatially dense velocity data within a cross section of a given flow geometry, which is difficult to obtain with any other measurement technique.

The DPIV technique has been extended to 3-D flow fields with scanning laser light sheets (Bruecker, 1995; Raffel et al., 1995). Recent imaging studies of the flow in porous media have demonstrated the potential application of the DPIV technique in complex geometries (Thovert and Adler, 1992). However, there is considerable room for improvement in the accuracy of measurements and subsequent image-processing calculations (see, e.g., Lourenco and Krothapalli, 1995).

In this article, we use the DPIV technique to measure the kinematics of viscous Newtonian and viscoelastic fluids. We perform our measurements on prototypical geometries encountered in polymer processing applications. The examples include rectilinear flow in a circular pipe, the flow past a sphere in a circular tube, the lid-driven cavity flow, and the extensional deformation of a liquid filament. These examples are motivated by common industrial applications involving pressure-driven fluid transport in circular conduits, coating processes, extrusion flows past die-forming elements, flow past obstructions, falling-ball rheometry, and fiber-spinning applications, as shown in Figure 1.

Our aim is to demonstrate the broad utility of the DPIV technique, not merely as a flow visualization tool, but as a technique for extracting important quantitative data in a planar cross section of a flow field. From this point of view, DPIV complements the LDV technique in many 2-D or ax-

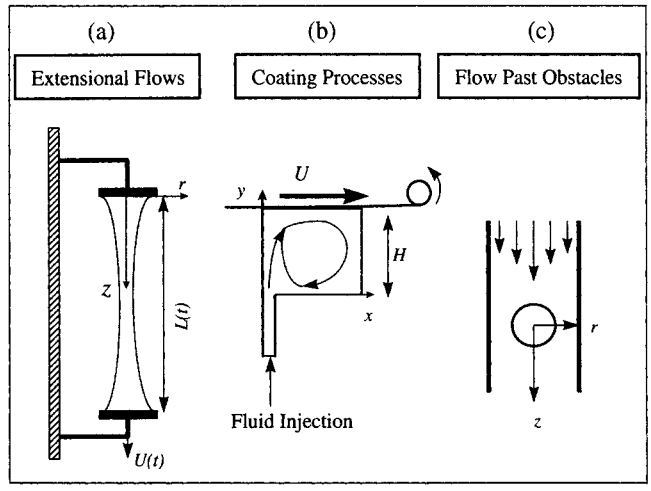

Figure 1. Three important flow processes in industrial applications.

The appropriate 2-D coordinate systems used in the experimental data are indicated for each geometry.

isymmetric, steady, and time-dependent flows of polymeric materials. To achieve this goal, we need to address the issue of velocity variation across a DPIV correlation region for dense-particle imaging experiments. We present a simple velocity-position assignment that provides quantitatively accurate discrete measurements of velocity fields. Rather than a detailed focus on the specific hydrodynamics of a single specialized flow configuration, we present representative data across a wide range of prototypical geometries of interest to engineers in the polymer processing industry. This includes planar and axisymmetric geometries, steady and transient flows, and problems involving a deformable fluid interface.

Many of these observations are entirely new and provide a clear indication of the broad utility of the technique. In the following section we consider the application of correlative imaging technique to viscoelastic fluids, and in the third section we discuss our algorithm for vector-position assignment and estimate the errors inherent to our implementation of the DPIV technique. In the fourth and fifth sections we provide details of the experimental test configurations and the rheology of the non-Newtonian test fluids. In the sixth section we present an overview of the key observations and results obtained for the wide range of flow geometries considered in this article.

Application in Viscoelastic Fluids

Polymeric fluids encountered in many industrial applications are highly viscous. The large magnitudes of the shear viscosity attenuate inertial effects, particularly in steady two-dimensional flow regimes. As a result of the relatively small magnitudes of the fluid velocity in many 2-D viscoelastic flows, low-cost digital image acquisition and storage systems are feasible with the speed of standard charge coupled device (CCD) cameras (30 frames/s). In transient viscoelastic flows the characteristic time scale for the flow is usually the relaxation time scale of the material, ($\lambda \sim O(s)$), which again can be resolved adequately with standard video frame rates. For flows with significantly smaller spatial and temporal scales (e.g., turbulent motion of fluids) it is necessary to utilize more sophisticated pulsed-light sources and photographic films (see, e.g., Adrian, 1991; Liu et al., 1991; Lourenco and Krothapalli, 1995).

Since the algorithm discussed here is correlative in nature, it is crucial to have a significant number of particles in each individual interrogation area in order to calculate a cross-correlation function that is representative of the average displacement of fluid particles. Polymeric materials can be seeded with higher concentrations of particles (typically up to a volume fraction of $\phi \approx 0.1\%$) before the effect of particle interaction and inertia become significant enough to affect the fluid rheology and the flow kinematics.

The cross-correlation function quantifies the "average shift" of illuminated regions in an interrogation area. Hence, the translation of solid bodies that are partially contained in an interrogation region can also be resolved adequately. This feature is important in resolution of flow fields around moving objects in a fluid medium. On the other hand, if the solid body is fixed in space with respect to the flow field, the cross-correlation shift that encompasses the fixed solid region does not accurately represent the local fluid motion. Since the images are stored digitally, however, it is possible to apply "region-of-interest" (ROI) masks to remove undesired static artifacts of the flow geometry, and correct for this solid boundary effect.

Viscoelastic flows in typical geometries of industrial interest are a complex combination of shear and extensional kinematics. In order to achieve sufficient resolution in a correlative technique, a large magnification of the flow field is necessary. In many flow processes, the magnitude of the velocity may be significantly greater in one direction than the other. In order to achieve adequate dynamic range and spatial resolution in both directions, we use nonsquare correlation regions.

In our implementation of the DPIV technique we take advantage of the viscous properties of viscoelastic fluids and we use a particle concentration of approximately 25 particles per 32×32 pixel regions, which is higher than the typical density used by Willert and Gharib (1991) and other investigators. In addition, when the fluid deformation has a preferred direction, we use rectangular correlation regions typically of 64×32 pixels, and rotate the image such that the principal axis of fluid motion lies along the longer side of the grid. Theoretically, a 64×32 interrogation region can resolve a maximum displacement of $\pm 32 \times \pm 16$ pixels. The theoretical upper bound for the maximum displacement is not usually valid under typical experimental conditions because particles leave and enter the correlation region nonsymmetrically.

In previous studies of DPIV (see, e.g., Willert and Gharib, 1991), overlapping interrogation regions have been used. To keep our implementation simple and the corresponding analysis systematic, we use overlapping correlation regions with step sizes of half of one grid dimension in each direction, which in the preceding example is 32 and 16 pixels, respectively.

To demonstrate the accuracy of our computer program and experimental technique, we show in Figure 2 the error determined from our DPIV analysis of a translated test image. The test image was generated by randomly placing white squares of 2×2 pixels on a black background of size 448×448

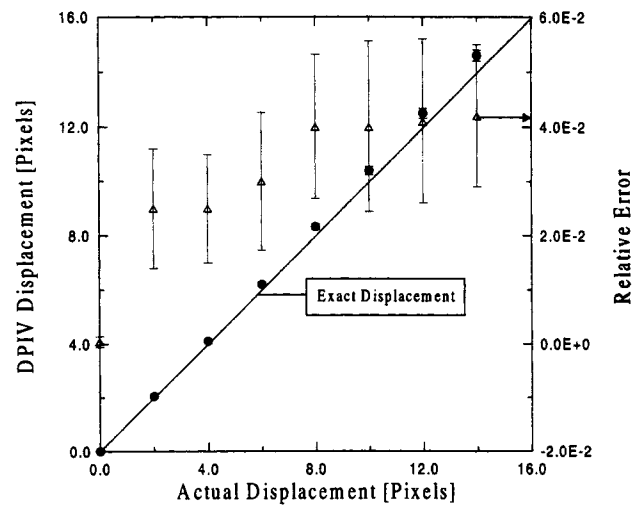

Figure 2. Error in the DPIV calculation for linear translations.

The correlation region is 32×32 pixels.

pixels. With a correlation region of 32×32 pixels, we achieve an approximate density of 20 particles per region. The test image was placed on a computer-controlled translating stage with a resolution of 1×10^{-3} mm, which at the video magnification of the experiment corresponds to a displacement of 5×10^{-4} pixels. The test image was translated at a constant speed and the images were acquired with a Panasonic GP-MF552 CCD camera at 1/30-s interval. Figure 2 shows the DPIV results vs. the exact displacement. The magnitude of the relative error, gradually grows as the maximum displacement of 16 pixels is reached. Displacement of ±10 pixels may be considered as the maximum experimentally attainable resolution for the chosen discretization. This is in agreement with similar tests by Willert and Gharib (1991).

In linear translation, velocity-position assignment is simple. However, in a two-dimensional flow in which the velocity field varies with the spatial position, locating the optimal placement position to generate a velocity grid can be difficult. Displacement vectors are usually displayed at the center of each calculation region. This assignment is not rigorous because theoretically, the displacement is the average displacement of the particles appearing in a subimage, and therefore should be placed at the center of mass of the ensemble of particles. However, calculation of the center of mass in a correlation region is not straightforward and can be very time-consuming.

In general, it is desirable to evaluate the velocity field in locations other than the center of rectangular grids. Eventually, an interpolation scheme has to be implemented; however, a brute-force interpolation on the original grids based on the center values has some degree of ambiguity because of the presence of overlapped regions. As indicated in Figure 3, there is a rectangular region of size $\Delta x/2\times\Delta y/2$ where four independent DPIV correlation regions overlap in the interior of the image.

If the particle density is high, it is reasonable to assume that the velocity determined by DPIV is a close approximation to the areal average of the fluid velocity in the subimage, or mathematically,

$$v_{\mathrm{DPIV}}(x)\approx\langle v\rangle_x=\frac{1}{S}\int_S v\,dS, \tag{1}$$

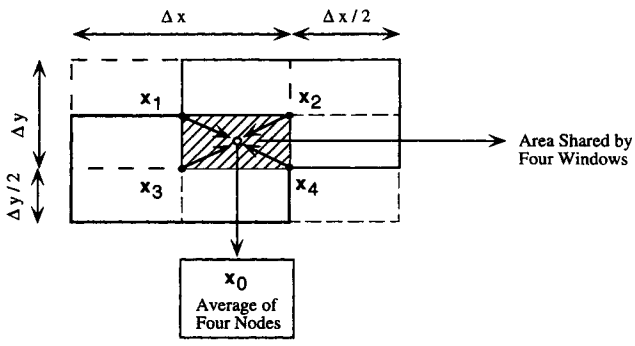

Figure 3. Four overlapping correlation regions of $\Delta x\times\Delta y$; the center of each region is labeled x_i, for $i=1$–4.

The intersection of the four correlation regions is shaded. The velocity vectors at $x_1\cdots x_4$ are averaged to calculate the velocity at x_0, which is the center of the shaded area.

where S is the area of the calculation region (or the grid), and $\langle\cdot\rangle_x$ indicates areal averaging centered at the point x. In the preceding estimate we further assume that as a result of the high data density the particle distribution is, and remains, symmetric about the origin of a rectangular correlation region on a pair of consecutive images.

We view the DPIV technique not merely as a flow visualization technique but as an algorithm that can capture accurate kinematic information about a flow field. Therefore, it is of particular interest to determine the positions where the computed velocity vectors should be assigned based on the assumption indicated in Eq. 1. The next section describes our approach to this issue.

Vector-Position Assignment

In a correlative technique such as DPIV, the velocity or the displacement field is assumed to be constant across the chosen correlation window. In actuality, for a deforming fluid, the velocity varies across the domain and there is a velocity gradient across each subimage. The velocity of a fluid element at a point x can be expanded in terms of the velocity field and its derivatives at another point, x_0, via the Taylor expansion

$$v(x)=v(x_0)+(x-x_0)\cdot\nabla v(x_0)+\frac{1}{2}(x-x_0)(x-x_0):\nabla\nabla v(x_0)+\cdots. \tag{2}$$

If we consider a rectangular interrogation region with x_0 located at the center, on areal averaging, the linear term (or odd terms in general) average to zero by symmetry:

$$\langle v\rangle_{x_0}=v(x_0)+\frac{1}{2}\langle(x-x_0)(x-x_0)\rangle_{x_0}:\nabla\nabla v(x_0)+\cdots. \tag{3}$$

Upon evaluation of the second moment, we obtain the estimate

$$v(x_0)=\langle v\rangle_{x_0}-\left(\frac{\Delta x^2}{24}\frac{\partial^2}{\partial x^2}+\frac{\Delta y^2}{24}\frac{\partial^2}{\partial y^2}\right)v(x_0)+\cdots. \tag{4}$$

If we treat Eq. 4 as an error formula for the dense DPIV technique, we observe that for rigid translation and linearly varying velocity fields, the error in each interrogation region is zero.

Figure 3 shows a diagram of a set of four interrogation regions that overlap on a rectangular subregion of size $(\Delta x/2\times\Delta y/2)$. Instead of placing the velocity vectors on the four nodes of the shaded area, we average the four nodal values and place the new averaged vector at x_0. In the interior of the image, this procedure creates a mesh of size $(N-1)\times(M-1)$ from a mesh of size $N\times M$.

The original $N\times M$ mesh is centered on a set of overlapping rectangular regions of size $\Delta x\times\Delta y$. The new mesh is on $(N-1)\times(M-1)$ *nonoverlapping* rectangular regions of size $\Delta x/2\times\Delta y/2$. We calculate the average velocity at the central point x_0 shown in Figure 3 by averaging the nodal values

$$\langle v\rangle_{x_0}=\frac{1}{4}\sum_{i=1}^{4}\langle v\rangle_{x_i} \tag{5}$$

$$=\frac{1}{4}\sum_{i=1}^{4}\left\{v(x_i)+\frac{1}{2}\langle(x-x_i)(x-x_i)\rangle_{x_i}:\nabla\nabla v(x_i)+\cdots\right\}.$$

We need to relate $\langle v\rangle_{x_0}$ calculated via Eq. 5 to $v(x_0)$ to estimate the leading error. The velocity at x_0 can be related to the nodal values order via the Taylor expansion

$$v(x_0)=\frac{1}{4}\sum_{i=1}^{4}\left\{v(x_i)+(x_0-x_i)\cdot\nabla v(x_i)\right.$$

$$\left.+\frac{1}{2}(x_0-x_i)(x_0-x_i):\nabla\nabla v(x_i)+\cdots\right\}. \tag{6}$$

For a linearly varying velocity field, ∇v is constant and Eq. 6 simplifies to the expected result:

$$v(x_0)=\frac{1}{4}\sum_{i=1}^{4}v(x_i).$$

For a higher order field, we can expand ∇v as

$$\nabla v(x_i)=\nabla v(x_0)+(x_i-x_0)\cdot\nabla\nabla v(x_0)+\cdots,$$

which upon substitution in Eq. 6 results in

$$v(x_0)=\frac{1}{4}\sum_{i=1}^{4}\{v(x_i)+(x_0-x_i)\cdot\nabla v(x_0)$$

$$+(x_0-x_i)(x_i-x_0):\nabla\nabla v(x_0)$$

$$\left.+\frac{1}{2}(x_0-x_i)(x_0-x_i):\nabla\nabla v(x_0)+\cdots\right\}.$$

We observe that

$$\sum_{i=1}^{4}(x_i-x_0)=0$$

by symmetry, which simplifies the previous result to

$$v(x_0)=\frac{1}{4}\sum_{i=1}^{4}\left\{v(x_i)-\frac{1}{2}(x_0-x_i)(x_0-x_i):\nabla\nabla v(x_0)+\ldots\right\}. \tag{7}$$

Upon rearrangement of Eq. 7 and substitution in Eq. 5 for the term $1/4\sum_{i=1}^{4}v(x_i)$, we obtain an approximate error formula for our vector placement procedure:

$$v(x_0)=\langle v\rangle_{x_0} \tag{8}$$

$$+\frac{1}{4}\sum_{i=1}^{4}\left\{\frac{1}{2}(x_i-x_0)(x_i-x_0):\nabla\nabla v(x_0)\right.$$

$$\left.+\frac{1}{2}\langle(x-x_0)(x-x_0)\rangle_{x_i}:\nabla\nabla v(x_i)+\cdots\right\}.$$

If we assume that $\nabla\nabla v$ is constant in our region of interest (which is exactly true for up to a quadratic flow field), the leading order error in the approximation is,

$$\begin{pmatrix}\frac{4\Delta x^2}{96} & \frac{\Delta x\Delta y}{32}\\ \frac{\Delta x\Delta y}{32} & \frac{4\Delta y^2}{96}\end{pmatrix}:\nabla\nabla v. \tag{9}$$

A separate additional cross-correlation calculation on a rectangular region of size $(\Delta x/2\times\Delta y/2)$ gives a leading order error of

$$\begin{pmatrix}\frac{\Delta x^2}{96} & 0\\ 0 & \frac{\Delta y^2}{96}\end{pmatrix}:\nabla\nabla v. \tag{10}$$

Equation 9 is slightly larger in magnitude than Eq. 10, but it preserves the leading order of error. The advantage of the averaging technique to direct calculation on the overlapping region is that with almost the same error, we can resolve a maximum displacement of $\pm\Delta x/2,\pm\Delta y/2$ on a correlation region of size $\Delta x/2\times\Delta y/2$.

Experimental Implementation

The experimental setup consists of a light source, optical lenses to create a thin light sheet, a CCD video camera, and a computer with an image processing board. A diagram of the experimental setup used in the present work is shown in Figure 4. In our experiment the light source is a low-power 300-mW Ar-ion laser. We use a single-mode optical fiber, manufactured by Oz Optics Inc., to permit flexible delivery of the illumination light. In addition, we use a non-Gaussian optical element to achieve uniform light intensity across the

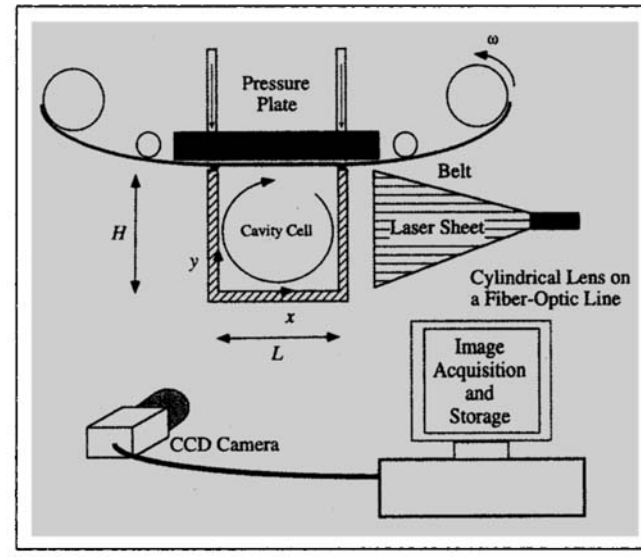

Figure 4. Experimental setup.

The 2-D flow field in the diagram is the driven cavity flow.

image. The beam width at the best focus is approximately 1 mm. The seeding particles are 50-μm silver-coated hollow glass spheres (Potter Industries, Inc.). The particle density is approximately 3,400 particles/cm^3 (corresponding to a volume fraction of 1.2×10^{-4}). Using Einstein's correction to the viscosity of a suspension (Batchelor, 1960),

$$\eta_{susp}/\eta_{solv} = 1+2.5\phi,$$

where η is the shear viscosity and ϕ is the volume fraction, we can expect an increase of approximately 0.06% in the shear viscosity of the test fluid. The concentration given earlier produces approximately 20–25 particles per correlation region of 32×32 pixels. Each particle occupies an image area of approximately 4–9 pixel^2 in the magnification range used in the problem.

Images from the CCD camera (Panasonic GP-MF552) are passed via an 8-bit digital video signal directly to a dedicated array processor (Dipix Corp. P360F), which operates on a personal computer (Micron PCI-90) equipped with a 90-MHz Intel Pentium processor. After storage onto the hard disk, the images are processed in subsequent frames and the evolving velocity fields were graphically displayed and numerically recorded. The processing time for each pair of frames is approximately 35 s, including interpolation to subpixelar accuracy.

As in any DPIV analysis, there are regions that either have weak correlation regions or do not contain any illuminated particles. To report a value in such regions, we used two strategies depending on the flow conditions; for steady flows, we calculate the value in the corresponding region of another pair of images from the same experimental run. For unsteady flows, we use the averaging of up to eight neighboring values, which has become a standard practice in DPIV analysis of images, and is sufficiently robust if the number of unacceptable vectors is low. This is always the case here as a result of the high seeding density.

Since the DPIV algorithm is correlative, moving solid boundaries that partially cover an interrogation region do not, in principle, introduce an error in the calculation of the average shift. We have been careful to customize our image-acquisition strategy so that only the interior of the fluid domain fits in an image to avoid the effect of stationary boundaries on correlation regions calculated near the bounding surfaces.

The DPIV technique is inherently a 2-D algorithm. In the presence of a significant out-of-plane motion, the accuracy of planar velocity calculations depends on the thickness of the light sheet, magnitude of the out-of-plane velocity component, the time difference between image acquisitions, and the light intensity distribution across the illuminated sheet. The analysis of such cases is beyond the scope of this article, although it is important for further extension of the technique to 3-D measurements (Raffel et al., 1995). In our experiments, we have been careful to apply the technique in 2-D flow regimes. The two-dimensionality of the flows was carefully verified with LDV measurements that scan the flow fields perpendicular to the DPIV plane of measurement.

Since out-of-plane motions result in translation of particles out of the imaging plane generated by the planar light sheet, there is an automatic loss of correlation between successive images. For the video-based algorithm and illuminating light sheet discussed here, the maximum tolerable out-of-plane velocity component is $v_{z,max} \sim 0.5$ mm/0.033 s ~ 1.5 cm/s. An *a-posteriori* check shows that the two-dimensionality of the computed velocity field can also be obtained by confirming that conservation of mass is satisfied across the flow region. An estimate of the out-of-plane velocity gradient is therefore

$$\frac{\Delta v_z}{\Delta z} \sim -\left[\left(\frac{\Delta v_x}{\Delta x}\right)+\left(\frac{\Delta v_y}{\Delta y}\right)\right].$$

Such an estimate is of course prone to experimental noise in the computation of the velocity gradients, but in the results presented here the out-of-plane velocity gradient is typically less than 10% of the maximum of the in-plane velocity gradient. Furthermore, across the entire planar flow field, the ratio,

$$\frac{\int_S \nabla\cdot\boldsymbol{v}\, dS}{\int_S (\nabla\boldsymbol{v})_{12}\, dS},$$

was usually smaller than 15%.

Fluid Rheology

Three fluids were used in the course of these experiments to highlight the complex effects of rheology on the kinematics of the fluid flow. A polybutene (PB) oil (Amoco Indopol H300) with a molecular weight of approximately 1,000 g/mole was used in the Newtonian flow measurements. To investigate the effects of a purely elastic contribution to the Newtonian base fluid, an ideal elastic fluid (Boger, 1977/78) was synthesized by dissolving 0.2 wt. % of high molecular weight polyisobutylene (PIB) (Exxon L-120, $M_w \sim 1.2\times10^6$ g/mole) in the same polybutene solvent. The rheology of the resulting "Boger fluid" was similar to the extensive experimental characterization of Quinzani et al. (1990). Although the fluid showed significant elastic behavior, as a result of the high viscosity solvent, shear thinning effects remained negligibly small over a wide range of shear rates, $0.01 < \dot{\gamma} < 100$ s^{-1}. To examine the importance of shear thinning effects, a 2 wt. % polyacrylamide (PAA) solution in a 50/50 mixture by weight of water and glycerol was also prepared. At room temperature, this solution demonstrated almost gel-like behavior with an extremely high shear viscosity; however, under typical flow conditions it exhibited significant shear-thinning effects.

The viscometric properties of these fluids are plotted in Figure 5. The shear viscosity of the Newtonian PB fluid was determined to be $\eta_s \approx 23$ Pa·s. The ideal elastic Boger fluid showed a similar, almost-constant viscosity of $\eta_0 \approx 25$ Pa·s over the same range of shear rates. The shear-thinning PAA solution had a zero-shear-rate viscosity of $\eta_0 \approx 464$ Pa·s and demonstrated appreciable shear-thinning effects beyond a shear rate of $\dot{\gamma} = 0.01$ s^{-1}. A nonlinear fit to the Carreau model,

$$\eta(\dot{\gamma}) = \eta_0[1+(\Lambda\dot{\gamma})^2]^{(n-1)/2}, \qquad (11)$$

with $n = 0.366$, $\Lambda = 118$ s, and $\eta_0 = 464$ Pa·s is plotted against the data, and provides a good description of the fluid rheol-

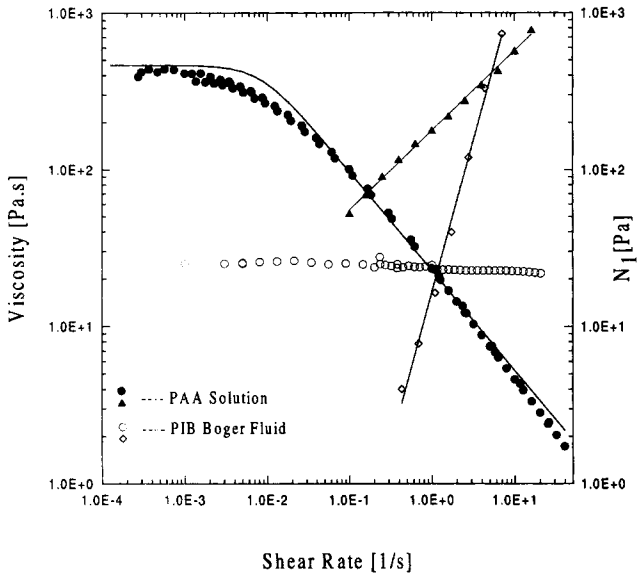

Figure 5. Viscometric properties for 2 wt. % PAA solution (solid symbols) and 0.3 wt. % PIB/PB solution (hollow symbols).

Circles show the viscosity, $\eta(\dot{\gamma})$ and triangles show first normal stress difference $N_1 = \Psi_1(\dot{\gamma})\dot{\gamma}^2$ measurements. The Boger fluid (PIB/PB solution) exhibits an almost constant viscosity and quadratic growth of the first normal stress difference. The PAA solution is shear thinning; the solid curve is fit to the Carreau model represented in Eq. 11 with $\eta_0 =$ 464 Pa·s, $\Lambda = 118$ s, and $n = 0.366$. The lines drawn through the N_1 data correspond to the values of $\Psi_1(\dot{\gamma})$ given in the text for each fluid.

ogy in steady shear. Here, $\eta(\dot{\gamma})$ is the shear viscosity, η_0 is the zero shear rate viscosity, and $\dot{\gamma}$ is the shear rate.

In the interest of brevity, details of the dynamic rheological data (η', η'') will not be presented; however, the normal force data, $N_1(\dot{\gamma}) = \Psi_1(\dot{\gamma})\,\dot{\gamma}^2$ is shown in Figure 5 for both PAA and PIB solutions. The first normal stress measurements for the ideal elastic Boger fluid exhibit a similar behavior to the measurements of Quinzani et al. (1990); the first normal stress coefficient, $\Psi_1 = N_1/\dot{\gamma}^2$, remains relatively constant at 45 Pa·s^2 in the shear rate range of $0.2 < \dot{\gamma} < 20$ s^{-1}, beyond which it shear thins. The first normal stress coefficient of the PAA solution exhibits significant shear thinning, which can be fit adequately by a power-law expression,

$$\Psi_1(\dot{\gamma}) = k\dot{\gamma}^{(m-2)},$$

with $k = 180$ Pa·s^m and $m = 0.54$.

An estimate of the characteristic relaxation time in the material can be obtained from viscometric properties in steady shear flow as (Bird et al., 1987),

$$\lambda(\dot{\gamma}) = \frac{\Psi_1(\dot{\gamma})}{2(\eta(\dot{\gamma}) - \eta_s)}.$$

For the Boger fluid the relaxation time is independent of the shear rate in the range of $0.2 < \dot{\gamma} < 20$ s^{-1} and has a value of $\lambda \sim 1.6$ s. However, for the shear thinning solution the time constant is shear-rate dependent and decreases from $\lambda \approx 50$ s at $\dot{\gamma} = 0.1$ s^{-1} to $\lambda \approx 0.1$ s at $\dot{\gamma} = 100$ s^{-1}.

Results

In order to highlight the utility of the DPIV technique in non-Newtonian fluid dynamics, we present four examples of flows in prototypical geometries encountered in polymer processing applications. The examples include flow through circular conduits, the flow field around a sedimenting sphere in a tube, the lid-driven cavity flow, and the extensional flow of a liquid filament. Our emphasis is on the utilization of the experimental technique across a broad range of conditions rather than detailed fluid mechanical analysis of these geometries, as each flow field by itself has been the subject of a wide range of previous theoretical and experimental investigations. However, many of the results and observations in non-Newtonian fluids presented here are entirely new and motivate further exploration and possible extensions of the DPIV technique.

Pipe flows

Fluid flow in circular conduits and pipes is one of the oldest problems in fluid mechanics and has many practical applications in fluid transport, diffusion, and heat transfer in industrial and biological settings. The well-known Hagen–Poiseuille equation for the flow of Newtonian fluids relates the volumetric flow rate to the pressure drop based on the analytical solution of Navier–Stokes equations in the laminar region (see, e.g., Bird et al., 1960).

For a generalized Newtonian fluid characterized by the Ostwald–de Waele power-law model, the velocity profile is

$$v_z = v_{z,\max}\left[1 - \left(\frac{r}{R}\right)^{(1/n)+1}\right], \tag{12}$$

where r and z are radial and axial positions in a cylindrical coordinate system, R is the radius of the pipe, and n is the power-law exponent (Bird et al., 1987). The maximum velocity, $v_{z,\max}$, is related to the axial pressure drop via

$$v_{z,\max} = \left(\frac{\Delta\rho R}{2\kappa L}\right)^{1/n}\frac{R}{1/n+1},$$

where ρ is the modified pressure, κ is the power-law consistency parameter, and L is the length of the tube. For $n = 1$ the fluid is Newtonian with a viscosity of $\kappa = \mu$, and the velocity profile is parabolic. For $n < 1$, the fluid is shear-thinning and the velocity profile is flatter in the middle

Figure 6 shows the steady velocity profile of a Newtonian viscous polybutene liquid ($\mu \approx 23$ Pa·s) in a circular pipe as measured by the DPIV technique. In this case, the pipe flow was generated by gravitational drainage of a reservoir through a transparent glass-walled tube. The pipe internal diameter in our setup was 2.5 cm. The measurements were performed approximately 5 diameters away from the entrance of the pipe to avoid any entrance effect; however, entrance effects and the evolution of a fully developed velocity field can also be studied using this technique. The position of the centroid of each subimage was distorted radially due to refraction through the curved surface. This distortion can be corrected in a straightforward manner using Snell's law of refraction.

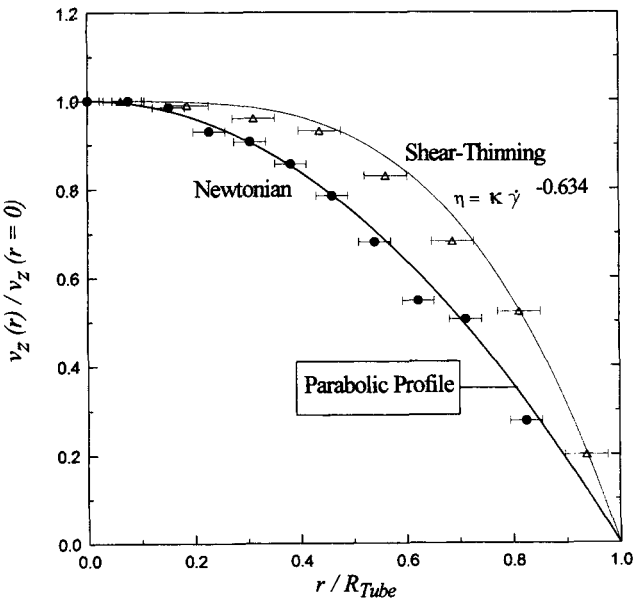

Figure 6. Axial velocity of the Newtonian polybutene fluid and polyacrylamide solution (shear-thinning) in a circular pipe measured by the DPIV technique.

The solid line through the non-Newtonian data is the velocity profile of a power-law fluid with the exponent of $n = 0.366$.

This optical correction does not affect the magnitude of the calculated velocity field whether it is performed before or after the cross-correlation calculation because, in this example, the velocity vector has only a single component in the axial z-direction. However, it will affect the apparent radial distribution of the axial velocity. In cases where the magnitude of the radial velocity is significant, DPIV image correction for refractive effects should be performed prior to cross-correlation calculations since it affects the magnitude of the calculated displacement, Δr, used to calculate the radial velocity component in each subimage window.

The measured Newtonian velocity profile matches the expected parabolic profile well, and is in sharp contrast with the velocity profile measured with the PAA solution. The PAA solution exhibits the effect of shear thinning by developing a significantly flatter velocity profile more similar to a plug flow. The solid line through the PAA data in Eq. 12 with a power-law coefficient of $n = 0.366$, which is obtained from the experimental fit to the viscometric data for the PAA solution. This simple and familiar one-dimensional (1-D) example is demonstrative of the information that can be generated from DPIV; however, the technique is of more use in complex two-dimensional flows, as illustrated in the next section.

Steady motion of a sphere

Fluid flow around solid objects is an important and extensively studied problem in suspension mechanics and classical treatise in fluid mechanics (e.g., Batchelor, 1960). Highlighted by the Stokes drag law and Stokes–Einstein relation, the detailed knowledge of flow around submerged particles can be used to predict the rheological and structural behavior of many complex microstructured materials (see, e.g., Russel et al., 1990). Understanding the motion of viscoelastic fluids around particles and drops also has very important applications in many practical industrial operations, as outlined in the recent text by Chhabra (1992). Variations of the viscometric and extensional properties of the fluid as functions of the local rate of deformation can result in substantially different fluid kinematics from those expected in Newtonian fluids (Walters and Tanner, 1992). Such modifications result in deviations from Stokes' law and inhibit the use of falling-ball rheometry as a simple technique for measuring the viscosity of polymer solutions.

Furthermore, with the advancement of numerical solutions of viscoelastic flows, the problem of a sphere settling in a tube filled with a viscoelastic fluid has evolved into a benchmark for the test of convergence of various numerical techniques (Brown et al., 1994). The lack of spatially dense kinematic data has limited the direct comparison of numerical results and experimental observations. To date most experimental comparisons have focused on either simple measurements of the drag coefficient or the velocity at a single point in the fluid domain (Arigo et al., 1996). Through this example we demonstrate that with DPIV, it is possible to make quantitative measurements of the full 2-D fluid kinematics in this flow geometery.

To quantify the magnitude of the non-Newtonian normal stresses in the steady sedimentation of a sphere through a viscoelastic fluid, we can define a Weissenberg number, Wi, as

$$Wi = \lambda\dot{\gamma} = \frac{\lambda U_s}{a},$$

where λ is the characteristic relaxation time of the fluid, U_s is the sphere's sedimentation velocity, and a is the sphere's radius. The full 2-D velocity field around a sedimenting sphere in a tube measured using our DPIV implementation is shown in Figure 7 at a Weissenberg number of $Wi = 2.76$. The ratio of the radius of the sphere to the radius of the tube is $a/R = 0.375$ and the selected fluid medium is the PAA shear-thinning solution.

Comparing the velocity field in front of and behind the sphere, we observe the presence of a "negative wake" at the rear of the sphere (Sigli and Coutanceau, 1977), which gives rise to an additional recirculating toroidal vortex with an axial velocity component in the opposite direction to that of the falling sphere. This phenomenon is entirely absent in the analogous flow of Newtonian fluids or in the upstream flow region ahead of the sphere.

Experimental studies of Sigli and Coutanceau (1977) and Bisgaard (1983) indicate that this negative wake effect is present for all sphere-tube ratios and is a phenomenon caused by the non-Newtonian fluid rheology. In particular there is a delicate and complex balance between shear thinning in the material functions $\eta(\dot{\gamma})$, $\Psi_1(\dot{\gamma})$, characterizing the shear flow near the equator of the sphere and the strain hardening in the extensional viscosity function characterizing the shearfree extensional flow in the wake of the sphere. Numerical studies with inelastic fluid models (e.g., Carreau model) or quasi-linear viscoelastic models (e.g., the upper-convected Maxwell

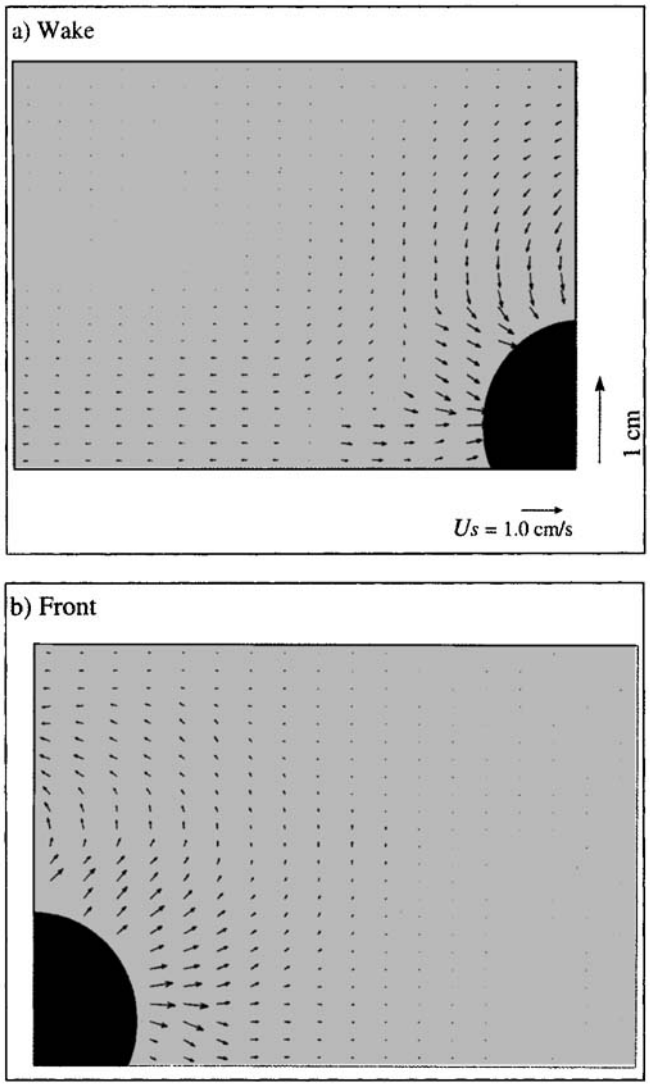

Figure 7. Flow field in (a) wake and (b) front of a sphere falling in a tube filled with the polyacrylamide shear-thinning solution.

The ratio of the radius of the sphere to the radius of the tube was $a/R = 0.385$. The settling velocity is $U_s = 1$ cm/s, and Weissenberg and Reynolds numbers are $Wi = 2.76$, $Re = 0.01$, respectively. The ratio of the density of the sphere to that of the fluid is $\rho_s/\rho_f = 2.45$. The motion of the sphere is from left to right.

model) do not show such a negative wake effect (Zheng et al., 1991); however, more recent computations with nonlinear constitutive models (Zheng and Phan-Thien, 1992; Harlen et al., 1995) were able to observe a negative-wake effect with a characteristic size and strength that depends on the magnitude of the respective nonlinear constitutive parameters. By quantitatively comparing the DPIV measurements presented in this article with such calculations, it will be possible to assess the validity of various micromechanical and continuum theories used to predict the kinematics and state of stress in the wake of objects. Such DPIV kinematical data provide a much needed piece of information for quantitative comparison with the computational results and can provide the necessary platform for numerical verification of selected rheological constitutive equations.

Cavity flows

The lid-driven cavity flow has become a classic model problem in Newtonian fluid mechanics because of its important applications in industrial coating flows (Aidun, 1991). While the literature on the cavity flow of Newtonian fluids is extensive, no detailed kinematic data on the effects of elasticity are available. Experimental results on the extent of mixing in time-periodic flows in the cavity geometry indicate that fluid elasticity has a significant effect on the geometrical structure of fluid path-lines (Leong and Ottino, 1990). Here, we provide the first quantitative observations of fluid kinematics in the cavity flow of an ideal elastic fluid.

First, we examine the velocity field in the cavity flow of a viscous Newtonian liquid. The cavity geometry was constructed of plexiglass with a cross section of 2.5×2.5 cm, and a length in the neutral direction of 10 cm. The cross-sectional area of size 2.5×2.5 cm was magnified by the video system to an image size of 416×416 pixels.

For comparison with the detailed kinematic measurements, the cavity flow of viscous Newtonian fluids was also computed numerically using a boundary integral technique (Pozrikidis, 1992). Figure 8 shows the x-component of velocity $v_x(y)$ along the vertical center line $x/H = 1/2$, of the cavity measured by DPIV, laser Doppler velocimetry (LDV), and through computation by boundary integral techniques. The DPIV correlation regions were of size 64×32 pixels, with 64 pixels aligned in the primary flow x-direction. The rectangular box in Figure 8 is shown to indicate the size of the individual correlation region. The experimental and computational results agree very well, even with an appreciable velocity gradient over each correlation region, which is demonstrative of the capabilities of our DPIV implementation. The

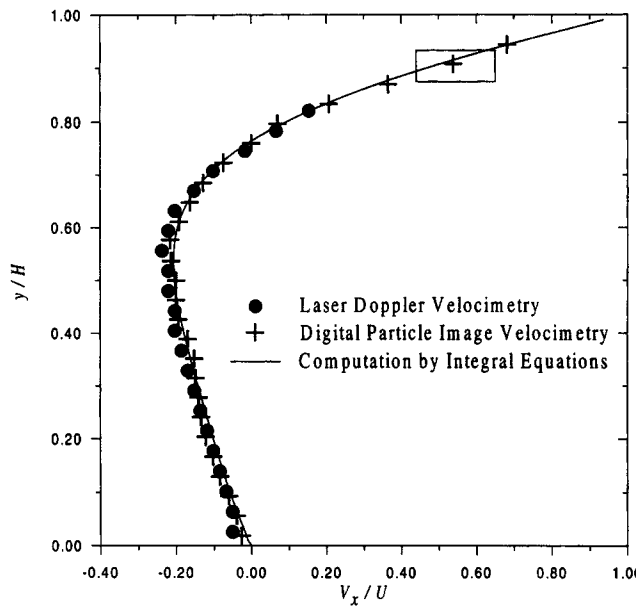

Figure 8. x-component of the velocity along the center line ($x = 0.5H$) of the driven cavity flow of the Newtonian polybutene fluid.

The comparison between laser Doppler velocimetry measurements, DPIV calculations, and computation by boundary integral equations is excellent; the size of the DPIV correlation region is indicated by the box.

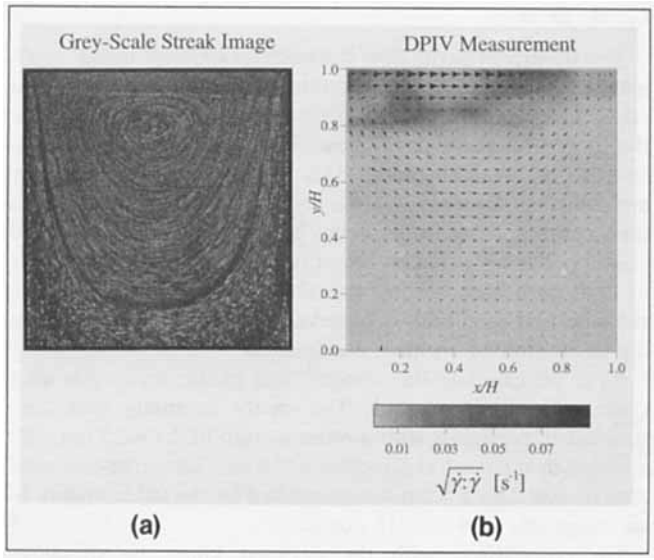

Figure 9. (a) Grey-scale streak image and (b) velocity field of the driven cavity flow for an ideal elastic Boger fluid superimposed on the magnitude of the second invariant of the velocity field shown in gray-scale intensity.

The Deborah number is $De = 0.20$ and the Reynolds number is $Re = 1.0\times10^{-3}$.

LDV measurements were obtained by scanning the LDV probe across the cavity in a series of steps and averaging 1,000 Doppler bursts at each point. By contrast, DPIV measures the complete 2-D kinematics in the cavity at each instant. This feature makes the technique useful for monitoring transient flows and onset of instabilities in such geometries as we show below.

Figure 9 shows a gray-scale streak image of the cavity flow of the ideal elastic fluid (PIB). The DPIV vector field is overlaid on a gray-scale image of the second invariant of the velocity gradient field, $\sqrt{\dot{\gamma}:\dot{\gamma}}$, where $\dot{\gamma} = (\nabla \boldsymbol{v}) + (\nabla \boldsymbol{v})^t$, and $\boldsymbol{v} = \{v_x, v_y\}$ is the 2-D velocity vector. The Reynolds number is defined as

$$Re = \frac{HU}{\nu},$$

where H is the horizontal width of the cavity, U is the linear speed of the top plate, and ν is the kinematic viscosity of the fluid. The maximum Reynolds number attained in the experiments is $Re = 6.0\times10^{-3}$, and hence inertial effects are negligible. The non-Newtonian elastic effects in the fluid are quantified by the Deborah number, which is defined as,

$$De = \frac{\lambda}{t_{\text{flow}}},$$

where λ is the relaxation time of the liquid, and t_{flow} is a characteristic time scale associated with the flow field. In this work, we take $t_{\text{flow}} = H/U$ as an appropriate measure of the residence time of fluid elements near the moving top plate.

Figure 9 presents the first detailed kinematic measurement of cavity flows of a viscoelastic fluid. The symmetry observed in the viscous Newtonian case is broken and the main core of the recirculation in the cavity is shifted slightly upstream. There are regions of large-velocity gradients near the upstream and downstream corners of the top plate. In these regions, the streamlines exhibit significant curvature, and fluid elements experience appreciable Lagrangian acceleration/deceleration. Our experiments indicate that a purely elastic instability is initiated at the downstream corner as the Deborah number increases beyond $De_{\text{crit}} = 0.35$, and the 2-D flow evolves into a cellular 3-D flow. The velocity gradients near the downstream corner intensify with increasing Deborah number, and coupled with the amplification of the viscoelastic hoop stress along the curved streamlines, they eventually lead to the onset of out-of-plane motion. The kinematic details of this elastic instability appear to be related to the formation of Taylor–Görtler-like vortices similar to those observed in viscoelastic flows through planar contractions (Chiba et al., 1995). Further details of the nonlinear dynamics of this instability are currently under investigation by the authors.

In Figure 10, the elastic recoil that develops in the cavity upon the cessation of the boundary motion is presented. In contrast with the slight shift of the main cell toward the upstream region during steady shearing motion at a velocity U, a recirculating motion with a center shifted toward the downstream corner is created after the top plate is stopped. In the case of viscous Newtonian flows, the fluid motion instantaneously ceases and the fluid, in general, does not show any recoil, since the molecules do not exhibit any memory effects of their deformation history. The observed elastic recoil in this non-Newtonian fluid will have a significant effect in mixing flows, and it must be partially responsible for the pronounced differences observed in the values of the extent of mixing between Newtonian and viscoelastic time-periodic

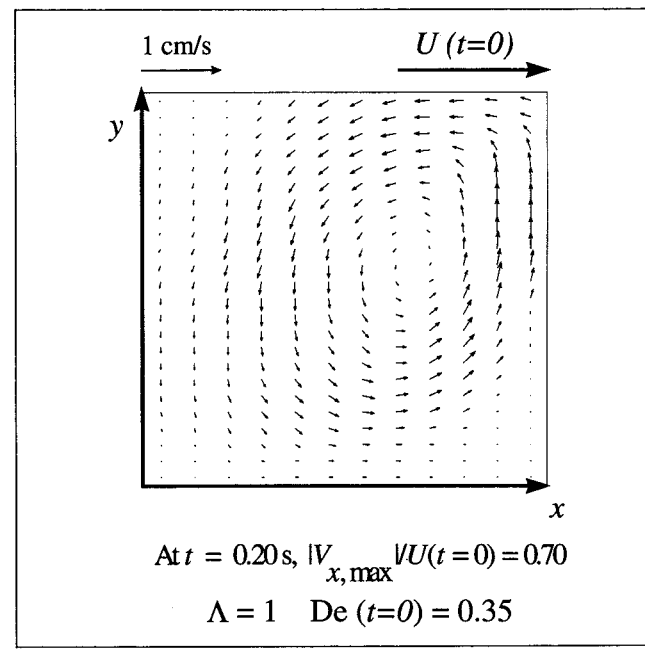

Figure 10. Elastic recoil upon the cessation of the steady flow.

The velocity field is measured at $t = 0.2$ s $\sim 0.125\lambda$ after the driving top lid was stopped.

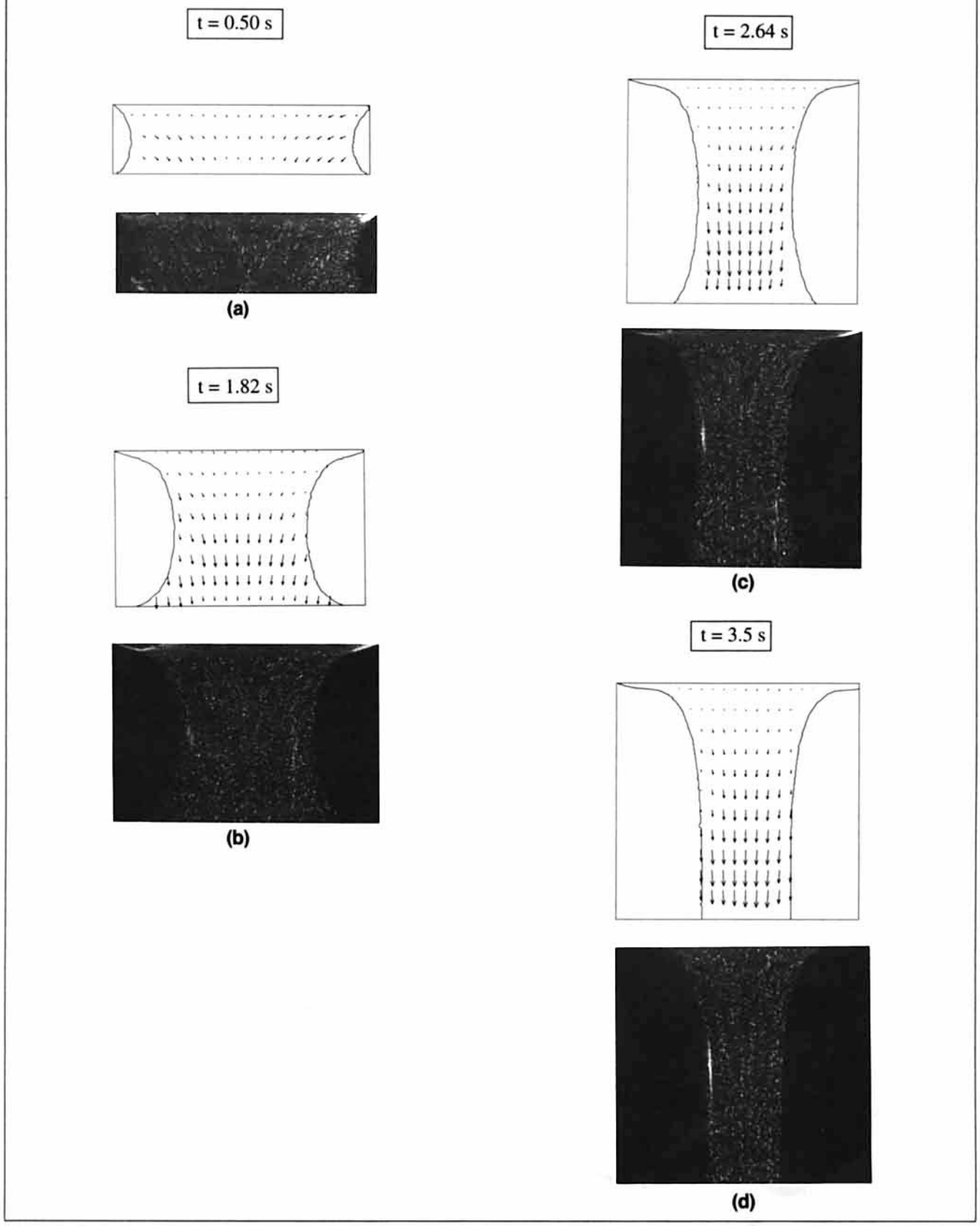

Figure 11. Time evolution of a polybutene Newtonian fluid filament during exponential stretching at a rate of $\dot{E} = 0.4$ s^{-1} and corresponding velocity fields measured by the DPIV technique.

(a) $t = 0.5$ s, $\epsilon = 0.2$; (b) $t = 1.82$ s, $\epsilon = 0.72$; (c) $t = 2.64$ s, $\epsilon = 1.06$; (d) $t = 3.5$ s, $\epsilon = 1.4$.

cavity flows previously reported by Leong and Ottino (1990). As they indicated in their flow-visualization mixing study, although the streamlines of the cavity flow of a Newtonian fluid in steady motion are very similar to the equivalent flow of a non-Newtonian Boger fluid, the extent of mixing is substantially lower in the time-periodic cavity flow of the Boger fluid. This observation is in agreement with our measurement of elastic recoil, since the geometry and kinematics of the recoil process are oriented against the general direction of the flow during the steady motion, and it should weaken the extent of mixing compared with the purely viscous time-periodic fluid motion in a similar geometry where memory effects are negligible.

Free surface motions: Liquid bridges

The extensional flow generated by exponentially stretching of liquid filaments has gained significant attention in light of the recent proposed stretching technique for the measurement of extensional viscosities of polymer solutions (Tirtaatmadja and Sridhar, 1993). By imposing an exponentially stretching flow field at the boundaries, $V_{\text{Plate}} = \dot{E}L_0 \exp(\dot{E}t)$, the hope is that the applied extension rate, $\dot{E}$, results in a homogeneous deformation within the fluid filament throughout the test, and measurements of the evolution in the tensile force at the end plates can be used to estimate the transient extensional viscosity of the non-Newtonian sample.

In the "liquid bridge" configuration, the kinematics are time-dependent and the flow has a free surface. Kinematic measurements with other techniques, such as LDV, in a free surface geometry, are extremely challenging (Matthys, 1988) and here, DPIV can provide a valuable tool to probe the fluid dynamics of these problems.

Figure 11 shows a series of images along with the corresponding DPIV analyses of the time evolution in the kinematics of the liquid bridge deformed at an imposed extension rate of $\dot{E} = 0.4\ \text{s}^{-1}$. The resulting Hencky strain (Bird et al., 1987) is denoted by $\epsilon = \dot{E}t = 0.4t$. In this experiment, the filament and the stretching apparatus are immersed in a vessel containing a low-viscosity fluid of the same density. The Bond number for the experiment is estimated to be $Bo = \Delta\rho g L_0/\sigma \approx 0.1$, where σ is the surface tension and L_0 is the initial length of the fluid column. This is the first sequence of kinematic measurements that provides insight into the applicability of the 1-D lubrication theory in the flow field generated by stretching a fluid filament by quantitatively measuring the uniformity of the velocity field across the liquid bridge. Figure 12 shows the axial velocity profile $v_z(r)$ at three different cross sections along the principal axis of extension. The axial velocity becomes increasingly uniform as we march closer to the moving plate, and the nonuniformity is more pronounced as the stationary plate is approached.

In Figure 13, the nondimensionalized axial velocity along the center line of the column ($r = 0$) is plotted against the axial position. The local fluid extension rate measured at every point inside the column is denoted,

$$\frac{\partial v_z}{\partial z} = \dot{\epsilon}(z).$$

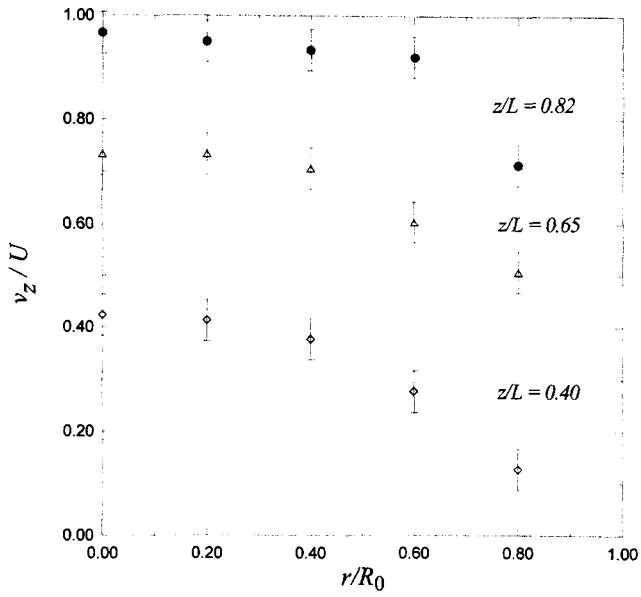

Figure 12. Axial velocity profile at three different axial positions along the principal axis of extension at a Henky strain of $\epsilon = 1.4$.

The axial velocity becomes increasingly uniform as the moving end plate is approached.

For homogeneous uniaxial extension, the measured value of $\dot{\epsilon}$ is independent of the axial position, and is equal to the imposed extension rate $\dot{E}$, which corresponds to the diagonal line in Figure 13. Our measurements indicate that the extension is in fact nonuniform and that the velocity gradient along

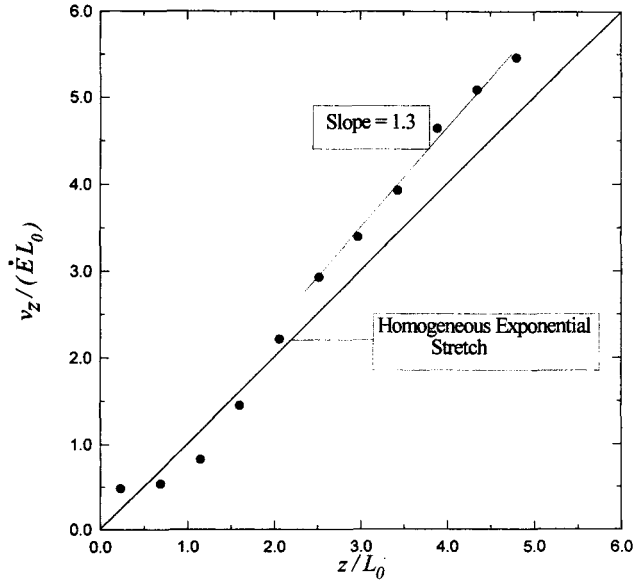

Figure 13. Axial velocity at the center of the liquid bridge nondimensionalized by the product of the extension rate and initial length of the column, $\dot{E}L_0$, as a function of the axial position.

The diagonal line indicates the desired homogeneous uniaxial elongation.

the center line is nonlinear. The extension rate near the axial midplane of the column is approximately 30% greater than the imposed extension rate, $\dot{E}$. This nonuniformity is present as a result of the no-slip boundary condition at the end plates. This results in the development of relatively stagnant "fluid reservoirs" at each end plate and an associated increase in the deformation rate near the axial midplane of the filament. This can be explained in detail by application of a lubrication approximation to the uniaxial extension of a liquid bridge (Spiegelberg et al., 1996). This analysis, valid for the limiting aspect ratio of $\Lambda_0 = L(t=0)/R_0 \ll 1$, predicts the measured midplane strain rate, $\dot{\epsilon}(z = 1/2L)$, should be 50% greater than the imposed elongation rate, $\dot{E}$. Our observations are performed at larger aspect ratios, $\Lambda(t) > 1$, which is beyond the limit at which the lubrication theory is valid, and remain to be verified using 2-D, time-dependent, free-surface flow numerical simulations.

Conclusion

We have demonstrated the broad applicability of a correlative particle-imaging algorithm, known as digital particle imaging velocimetry (DPIV), in viscoelastic flows where the kinematics are relatively slow and the particle concentration is higher than previously reported values. We have presented a simple averaging technique that creates a highly resolved velocity grid across an image and preserves the order of error based on an area-averaging assumption. The range and variety of industrially pertinent examples reveal the potential application of the technique in a host of complex flow geometries of interest in chemical engineering applications of non-Newtonian fluids, including closed systems (e.g., short-dwell cavities and coating flows), open flows (e.g., pipe flow, flow around obstructions), and free-surface, time-dependent flows (e.g., fiber-spinning, extrusion, and extensional flows). The extension of the technique to autocorrelative calculations based on multiply exposed single photographs generated by pulsed laser techniques, can also enable DPIV to measure faster fluid motions in densely seeded viscoelastic fluids.

The technique is particularly suitable for probing the spatial characteristics of flows that give rise to elastic hydrodynamic instabilities in conjunction with established time-series analysis techniques such as laser Doppler velocimetry (LDV); DPIV provides details of the velocity gradients and the geometrical structure of the flow on discrete planar cross sections, and LDV provides the faster temporally resolved information to quantify the transient evolution of the flow and the main modes of time-dependent elastic instabilities.

Acknowledgments

GHM gratefully acknowledges the financial support of National Science Foundation by an NYI award. The authors are grateful to Dr. Stephen H. Spiegelberg and Mr. Mark T. Arigo of Harvard University for their invaluable assistance in conducting the fluid-flow experiment.

Literature Cited

Adrian, R. J., "Particle-Imaging Techniques for Experimental Fluid Mechanics," *Ann. Rev. Fluid Mech.*, **23**, 261 (1991).

Aidun, C. K., "Principles of Hydrodynamic Instability: Application in Coating Systems, Part 2: Examples of Flow Instability," *TAPPI J.*, **74**(3), 213 (1991).

Arigo, M. T., D. Rajagopalan, N. Shapely, and G. H. McKinley, "The Sedimentation of a Sphere Through an Elastic Fluid. Part 1. Steady Motion," *J. Non-Newtonian Fluid Mech.*, **60**, 225 (1995).

Batchelor, G. K., *An Introduction to Fluid Dynamics*, Cambridge Univ. Press, Cambridge, England (1985).

Binding, D. M., K. Walters, J. Dheur, and M. J. Crochet, "Interfacial Effects in the Flow of Viscous and Elastoviscous Liquids," *Phil. Trans. R. Soc. Lond.*, **323**(A), 449 (1987).

Bird, R. B., R. C. Armstrong, and O. Hassager, *Dynamics of Polymeric Liquids*. Vol. 1: *Fluid Mechanics*, 2nd ed., Wiley Interscience, New York (1987).

Bird, R. B., W. E. Stewart, and E. N. Lightfoot, *Transport Phenomena*, Wiley, New York (1960).

Bisgaard, C., "Velocity Fields Around Spheres and Bubbles Investigated by Laser-Doppler Anemometry," *J. Non-Newtonian Fluid Mech.*, **12**, 283 (1983).

Boger, D. V., "A Highly Elastic Constant-Viscosity Fluid," *J. Non-Newtonian Fluid Mech.*, **3**, 87 (1977/78).

Boger, D. V., and K. Walters, *Rheological Phenomena in Focus*, Elsvier, New York (1993).

Brigham, E. O., *The Fast Fourier Transform*, Prentice Hall, Englewood Cliffs, NJ (1974).

Brown, R. A., and G. H. McKinley, "Report on the VIIIth International Workshop on Numerical Methods in Viscoelastic Flows," *J. Non-Newtonian Fluid Mech.*, **52**, 407 (1994).

Bruecker, C., "Digital-Particle-Image-Velocimetry (DPIV) in a Scanning Light-Sheet: 3D Starting Flow around a Short Cylinder," *Exp. in Fluids*, **19**, 255 (1995).

Buchhave, P., "Particle Image Velocimetry—Status and Trends," *Exp. Therm. Fluid Sci.*, **5**, 586 (1992).

Chen, Y., H. T. Davis, and C. W. Macosko, "Wetting of Fiber Mats for Composites Manufacturing: I. Visualization Experiments," *AIChE J.*, **41**(10), 2261 (1995).

Chhabra, R. P., *Bubbles, Drops, and Particles in Non-Newtonian Fluids*, CRC Press, Boca Raton, FL (1992).

Chiba, K., R. Ishida, and K. Nakamura, "Mechanism for Entry Flow Instability Through a Forward-Facing Step Channel," *J. Non-Newtonian Fluid Mech.*, **57**(2–3), 271 (1995).

Cho, Y.-C., "Digital Image Velocimetry," *Appl. Opt.*, **28**(4), 740 (1989).

Crochet, M. J., "Numerical Simulation of Highly Viscoelastic Flows," *Proc. Int. Cong. on Rheology*, Vol. 1, Sydney, p. 19 (1988).

Elliot, D. F., and K. R. Rao, *Fast Transforms: Algorithms, Analyses, Applications*, Academic Press, New York (1982).

Federal Coordinating Council for Science, Engineering, and Technology, "Advanced Material and Processing: The Fiscal Year 1994 Federal Program," National Institute of Standards and Technologies, Gaithersburg, MD (1993).

Harlen, O. G., J. M. Rallison, and P. Szabo, "A Split Lagrangian-Euler Method for Simulating Transient Viscoelastic Flows," *JNNFM*, **60**, 81 (1995).

Keunings, R., M. J. Crochet, and M. M. Denn, "Profile Development in Continuous Drawing of Viscoelastic Liquids," *Ind. Eng. Chem. Fund.*, **22**(3), 347 (1983).

Leong, C. W., and J. M. Ottino, "Increase in Regularity by Polymer Addition During Chaotic Mixing in Two-Dimensional Flows," *Phys. Rev. Lett.*, **64**(8), 874 (1990).

Liu, Z.-C., C. C. Landerth, R. J. Adrian, and T. J. Hanratty, "High Resolution Measurement of Turbulent Structure in a Channel with Particle Image Velocimetry," *Exp. Fluids*, **10**, 301 (1991).

Lourenco, L., and A. Krothapalli, "On the Accuracy of Velocity and Vorticity Measurements with PIV," *Exp. Fluids*, **18**, 421 (1995).

Matthys, E. F., "Measurement of Velocity for Polymeric Fluids by a Photochromic Flow Visualization Technique: The Tubeless Siphon," *J. Rheol.*, **32**(8), 773 (1988).

McKinley, G. H., P. W. Raiford, R. A. Brown, and R. C. Armstrong, "Nonlinear Dynamics of Viscoelastic Flow in Axisymmetric Abrupt Contractions," *J. Fluid Mech.*, **223**, 411 (1991).

Pozrikidis, C., *Boundary Integral and Singularity Methods for Linearized Viscous Flow*, Cambridge Univ. Press, Cambridge, England (1992).

Quinzani, L. M., G. H. McKinley, R. A. Brown, and R. C. Armstrong, "Modeling the Rheology of Polyisobutylene Solutions," *J. of Rheol.*, **34**, 705 (1990).

Raffel, M., M. Gharib, O. Ronneberger, and J. Kompenhans, "Feasi-

bility Study of Three-Dimensional PIV by Correlating Images of Particles within Parallel Light Sheet Planes," *Exp. Fluids*, **19**, 69 (1995).
Rajagopalan, D. R., M. T. Arigo, and G. H. McKinley, "Sedimentation of a Sphere Through an Elastic Fluid: Part II Transient Motion," *J. Non-Newtonian Fluid Mech.*, **00** (1996).
Russel, W. B., W. R. Schowalter, and D. A. Saville, *Colloidal Dispersions*, Cambridge Univ. Press, Cambridge, England (1987).
Scheller, B. L., and D. W. Bousfield, "Newtonian Drop Impact with a Solid Surface," *AIChE J.*, **41**(6), 1357 (1995).
Sigli, D., and M. Coutanceau, "Effect of Finite Boundaries on the Slow Laminar Isothermal Flow of a Viscoelastic Fluid Around a Spherical Obstacle," *J. Non-Newtonian Fluid Mech.*, **2**, 1 (1977)
Spiegelberg, S. H., D. C. Ables, and G. H. McKinley, "Measurements of Extensional Viscosity for Viscous Polymer Solutions with a Filament Stretching Rheometer," *J. Non-Newtonian Fluid Mech.*, **64**(2–3), 229 (1996).
Tirtaatmadja, V., and T. Sridhar, "A Filament Stretching Device for Measurement of Extensional Viscosity," *J. Rheol.*, **37**, 1081 (1993).
Walters, K., and R. I. Tanner, "The Motion of a Sphere Through an Elastic Liquid," *Transport Processes in Bubbles, Drops, and Particles*, R. P. Chhabra et al., eds., Hemisphere, New York, p. 73 (1992).
Willert, C. E., and M. Gharib, "Digital Particle Image Velocimetry," *Exp. Fluids*, **10**, 181 (1991).
Zheng, R., and N. Phan-Thien, "A Boundary Element Simulation of the Unsteady Motion of a Sphere in a Cylindrical Tube Containing a Viscoelastic Fluid," *Rheol. Acta*, **31**, 323 (1992).
Zheng, R., N. Phan-Thien, and R. I. Tanner, "The Flow Past a Sphere in a Cylindrical Tube: Effects of Inertia, Shear-thinning and Elasticity," *Rheol. Acta*, **30**, 499 (1991).

Manuscript received Jan. 29, 1996, and revision received Aug. 26, 1996.